Data Repository and Supplementary Materials for

Ice cover as a control on the morphodynamics and stratigraphy of Arctic deltas

YeJin Lim[1]*, Joseph S. Levy[2], Timothy A. Goudge[1], and Wonsuck Kim[1]**

[1]*Jackson School of Geosciences, University of Texas at Austin, Austin, TX 78712, USA*

[2]*University of Texas Institute for Geophysics, Austin, TX 78758, USA*

[**]*Now at Colgate University, 13 Oak Drive, Hamilton, NY 13346*

*Corresponding author E-mail: yjlim322@utexas.edu

CONTENTS OF THIS FILE

INTRODUCTION

This document provides additional information regarding (1) our experimental setup and parameters; (2) final delta deposits from each experiment; (3) vertical sections of each delta deposit; (4) bathymetric contours on each delta deposit; (5) lobe building timescales associated with sub-ice channel progradation; (6) ice-sediment interaction based on relative sediment discharges; (7) effective ice thickness for depth normalization; (8) derivation of roughness to quantify contour roughness changes over depth; (9) bathymetric maps and roughness plots for deltas in the natural system; and (10) time-lapse movies of delta formation taken through the glass-bottom of the experimental basin.

SUPPLEMENTARY TEXT

Supplementary Text 1: Extended description of experimental design and methods

We conducted three sets of 3D tank laboratory experiments (set 1 and 2 are included in the main text, and set 3 in the supplementary). Each set was composed of two experiments (Table DR1): one with ice cover in the receiving basin and the other under ice-free conditions. The tank (Fig. DR1) used in the experiments is 90 cm long, 44 cm wide, and 36 cm deep, and was placed at a slope of ~5°. Sediment and water were fed from a single point source into the basin with a constant water level. Due to the basin slope, water depth linearly increased from 4.2 cm at the upstream end to 12 cm at the downstream end. Sediment discharge was constant throughout sets 1 and 2 at 0.503 cm^3/s and 0.228 cm^3/s, respectively, while sediment discharge was increased from 0.228 cm^3/s to 0.503 cm^3/s after 1 hour (2/3 of the experimental duration) in set 3. Water discharge was held constant throughout all 6 experiments at 15.14 cm^3/s. Sediment was a mixture of brown crushed walnut shells (D = 74–250 μm, ρ = 1.3 g/cm^3) and white quartz sand (D = 170–200 μm, ρ = 2.65 g/cm^3) in a 2:1 ratio by volume to serve as proxies for fine- and coarse-grained sediments, respectively (Kim et al., 2006; Martin et al., 2009). The different colors of the two sediment types in the mixture also accentuated the contrast between them, allowing a better visualization of sediment transport and deposition in stratigraphic sections (Martin et al., 2009).

For experiments under ice-free conditions, we used water at room temperature (~19.5°C) to both fill in and supply the basin. For experiments with an ice cover, the water temperature was ~3°C, which is comparable to, although slightly cooler than, the measured spring water temperatures on the North Slope (U.S. Geological Survey, 2018). To simulate shorefast ice in which sea ice is frozen to the shore that is typical in the Arctic and in lake ice cover in Antarctica

(Are and Reimnitz, 2000), a 45.8 cm long, 44 cm wide, and 7 cm thick floating ice cover composed of pressed crushed ice was placed at the upstream end of the tank. A 10 cm by 10 cm area of this ice cover was carved out at the source to guide initial flow and to assist sediment deposition into open-water conditions. During delta deposition, the floating ice became frictionally coupled to the growing sediment surface. The ice cover was held in place with two bricks 45.8 cm downstream of the input source throughout the experiments. These bricks were also used in experiments without ice cover to ensure that no changes in basin geometry affected the deposits.

The run time for each experiment was 1 hour, 2 hours, and 1.5 hours for sets 1, 2, and 3, respectively, in order to ensure the same total amount of sediment enters the basin throughout the course of the experiment. Time-lapse photography with an overhead camera connected to a computer automatically captured delta surface morphology evolution (Tal et al., 2012) every 15 seconds during the entire duration of the experiments. In order to overcome and enhance the limited surface visibility caused by the ice cover and also by basin water that became murky due to suspended fine-grained sediments, a second camera was placed below the tank and simultaneously captured delta evolution every 60 seconds during each experiment.

At the end of each experiment, the water from the basin was drained to examine the morphology of the resultant deposit (Fig. 1a-b, Fig. DR2). For the ice-covered experiments, we waited until the ice cover was completely melted before draining the basin water. Topographic scans of each deposit were collected using a white-light scanning system after the draining of the basin. To study the deposit stratigraphy, half of the deposit was vertically sectioned in the radial direction (Fig. 2a-c, Figs. DR3-5) and the other half was sectioned horizontally in 0.5 cm to 1 cm increments down from the initial water level using a projected laser line (Fig. 4a-b, Fig. DR6A-F). All of the stratigraphic sections were imaged (Fig. 2a-c, Figs. DR3-6).

We corrected the images for distortion associated with camera lens curvature and perspective, so that all measured distances and areas are equivalent to measurements made on orthorectified images (Tal et al., 2012). Each original image had 4752 by 3168 pixels with a resolution of 28.35 pixels/cm. We converted the resolution to 10 pixels/mm for the analysis presented in the paper. Shoreline and delta toe positions were mapped onto images of each final deposit (Fig. 1a-b, Fig. DR2) in order to calculate the subaqueous delta distance, as well as the shoreline and toe line rugosities (Fig. 1c-d, Figs. DR7-8).

Images of the vertical stratigraphic sections were further processed in order to determine the 3D distribution of sediment within the deposits. First, each image was rotated and corrected for the accurate spatial coordinates with respect to the source point and the basin water level. Then, the area outside the deposit and the initial subaqueous fan near the source inlet was masked out to only consider the deltaic deposits for further analysis. These images were used to calculate the total thickness of the deposit within each section. We then created another set of images in grayscale, which was converted into binary images of black and white, using a quantitative thresholding technique (Tal et al., 2012) to identify areas dominated by the crushed walnut shells (white) and sands (black) in each image. The proportions of the two grain sizes in each deposit (Fig. 2d-e, Fig. DR9) were calculated using the binary set of images.

Images taken through the glass bottom of the basin during the experiments were used to map delta toe progradation over time (Fig. 3, Fig. DR10). Original images from the ice and ice-free experiments with high sediment discharge had 4000 by 3000 pixels and 1440 by 1080 pixels, respectively. The original resolution of 28.35 pixels/cm was converted to 10 pixels/cm to map toe locations over time. The toe distances were measured from the apex along stratigraphic sections whose locations were determined by overlapping of the final deposit images showing locations of all transects (Fig. DR4). These time series data were filtered using a high-pass 5th order Butterworth filter for signal processing. Edge frequencies of 0.05 and 0.4 cycles/min were used for data from ice-covered and ice-free experiments, respectively. The detrended filtered frequency spectra were used to compute the timescale for delta toe progradation (time= 1/frequency). The sampling interval used was 1 minute of run time.

Images of horizontal stratigraphic sections (Fig. 4a-b, Fig. DR6 A-F) were used to map and measure the length of depth contour lines (Ls_m). The cumulative area within each bathymetric contour (A_m) was also measured on these images. To quantify contour roughness changes with depth, we used a ratio of the measured contour line length (Ls_m) to the isometric line length (Ls_i, the length of a radially-symmetric contour line) (Wolinsky et al., 2010). Here, the isometric line length Ls_i is defined as $2\sqrt{A_m \alpha \pi}$, where α denotes the opening angle of the measured area as a fraction of 2π radians (see Text S2 for derivation).

For deltas in the natural system, many different sources were utilized for bathymetric data. For Colville and Mississippi River deltas, the digital elevation model (DEM) of Southern Louisiana (Love et al., 2010) was resampled to 500 m/px and international bathymetric chart of the Arctic Ocean (IBCAO) (Jakobsson et al., 2012) at 500 m/px were projected into the appropriate UTM zone projection in ESRI's ArcMap geographic information system (GIS) software and were clipped to the delta region of interest (Fig. 4e-f). Contour lines were calculated at an interval spacing roughly scaled to channel depth (1 m for Colville, 10 m for Mississippi River delta) in ArcMap. For Mackenzie and Yukon River deltas, we used bathymetric and fishing maps obtained from the National Centers for Environmental Information

(NCEI) of National Oceanic and Atmospheric Administration (NOAA) (Fig. DR13A-B). Additionally, we retrieved data and maps from the literature (Rodriguez et al., 2000; Davis and Dalrymple, 2012; Shaw et al., 2016) for ice-free deltas (Fig. DR14A-F), and used the contour spacing given by the acquired maps. For both Arctic and temperate deltas, the area limits and opening angles were determined by associating active deltaic distributary channels and their deposit boundaries. The contour lines and the bounding lines were merged to create a delta wedge, and were transformed into polygons so that area between each contour could be calculated. Multiple polygons in different locations were created within each delta in order to avoid subjectivity and be inclusive in choosing delta wedges. The angle subtended by the wedge (i.e., opening angle, α), contour line length (Ls_m), and the area within each contour (A_m) was measured for each polygon. These values then were used to compute the isometric line length (Ls_i) using the method outlined above. These equivalent contour lengths were then compared to the actual contour length measured within the polygon to calculate roughness (R).

For natural deltas, water depth values were normalized by the sum of effective ice thickness (T_i, the thickness of ice cover below the sea level that is actively interacting with the delta surface) and channel depth (T_c) at the river mouth ($D_{n_i} = \frac{D_i}{T_i+T_c}$, where D_{n_i} is normalized depth at depth i, and D_i is depth i). The values of ice thickness (ICESat; (Kovacs, 1981) and channel depth (Coleman, 1969; Mellor, 1983; Rodriguez et al., 2000; Hill et al., 2001; Saito et al., 2001; Chikita et al., 2002; Dalrymple et al., 2003; Bouchez et al., 2011; Shaw et al., 2016) for natural deltas were retrieved from the literature. For each experimental ice-covered delta, the average value of effective ice thicknesses measured on the images of the stratigraphic sections was used. The channel depth was estimated to be 3 mm for all experimental deltas (Table DR2 for the values used for each delta).

Supplementary Text 2: Surface roughness derivation

Images of horizontal stratigraphic sections (Fig. 4a-b, and Fig. DR6A-F) were used to map and measure the length of depth contour lines (Ls_m). The cumulative areas within each bathymetric line (A_m) were also measured on these images.

To quantify contour roughness changes over depth, we used a ratio of the measured contour line length (Ls_m) to the isometric line length (Ls_i, the length of a radially-symmetric contour line) (Wolinsky et al., 2010):

$$Roughness = {L_{s_m}}/{L_{s_i}} \tag{1}$$

The isometric line length was computed by calculating a radius of a circle with an equivalent area following the calculation steps below. First, the measured area, A_m, was calculated by:

$$A_m = \alpha\pi r^2 \tag{2}$$

where α = opening angle of measured area as a fraction of 2π radians. We can then solve for r to calculate the radius of a circle with an equivalent area:

$$\therefore r = \sqrt{{A_m}/{\alpha\pi}} \tag{3}$$

The isometric line length, L_{s_i}, can be computed by:

$$L_{s_i} = 2\alpha\pi\mathrm{r} \tag{4}$$

Substituting r to calculate isometric line length with an equivalent area:

$$L_{s_i} = 2\alpha\pi\ \left(\sqrt{{A_m}/{\alpha\pi}}\right) \tag{5}$$

$$\therefore L_{s_i} = 2\sqrt{A_m\alpha\pi} \tag{6}$$

Figure Data Repository 1.

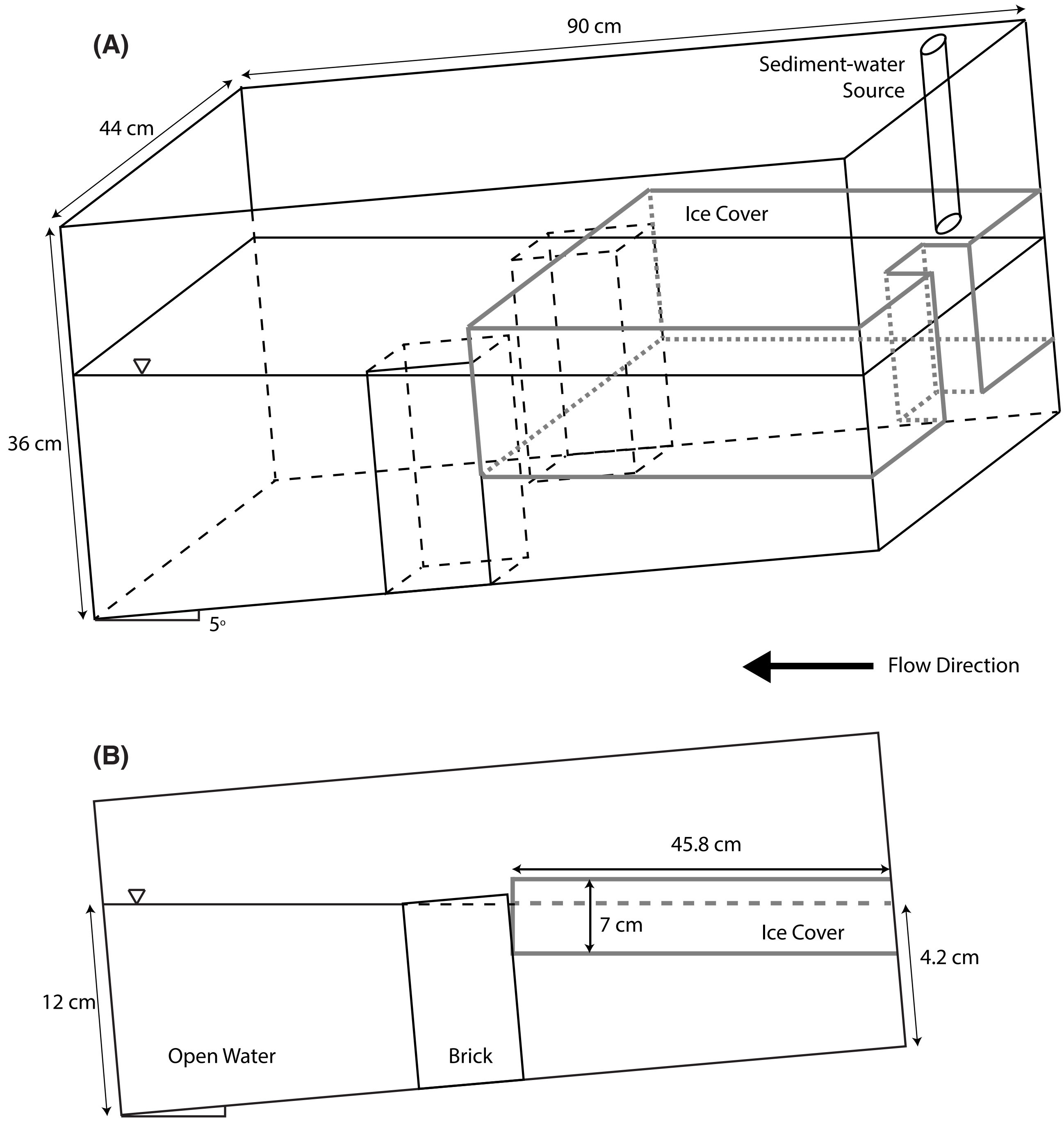

Figure Data Repository 2.

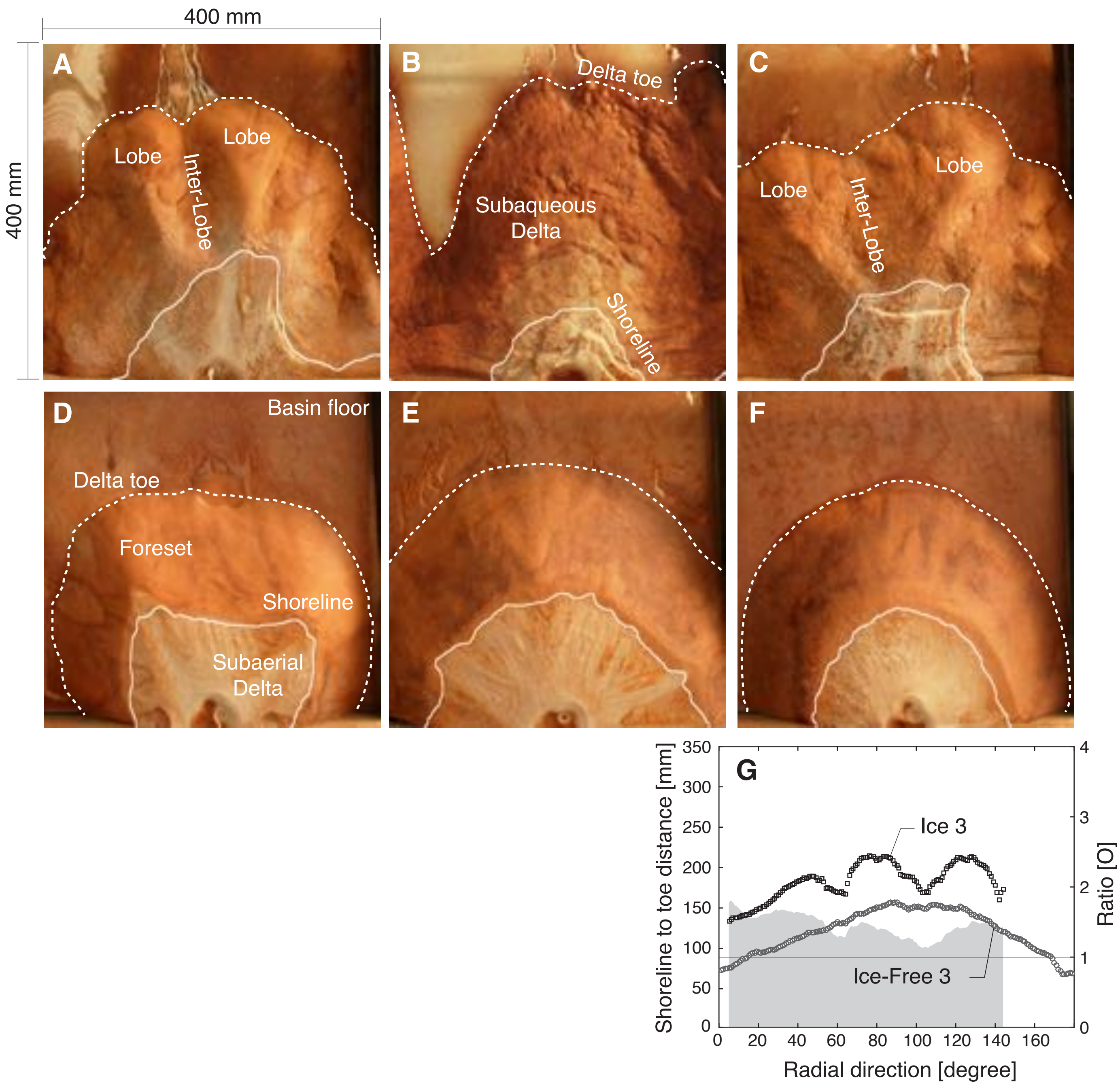

Figure Data Repository 3.

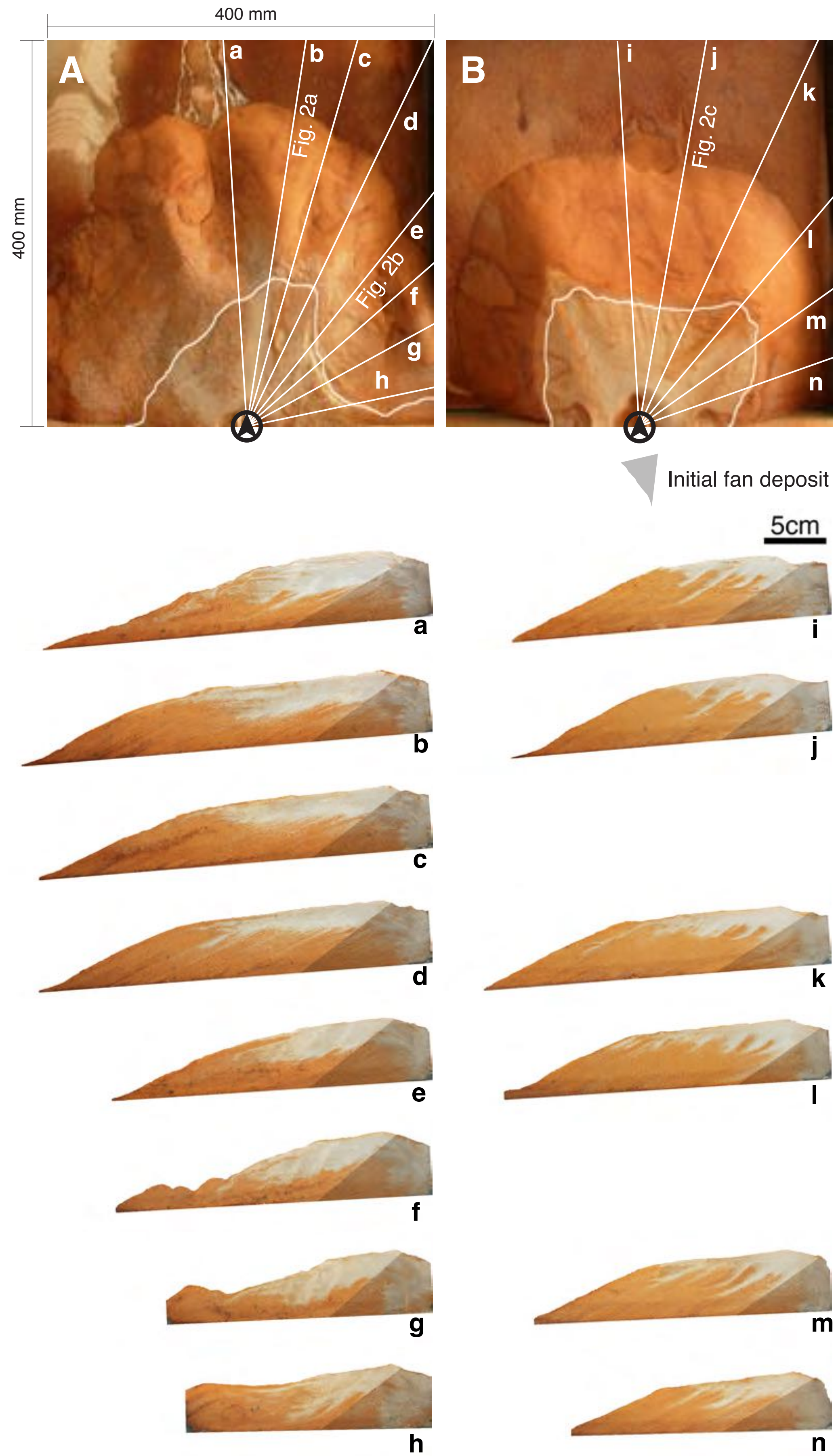

Figure Data Repository 4.

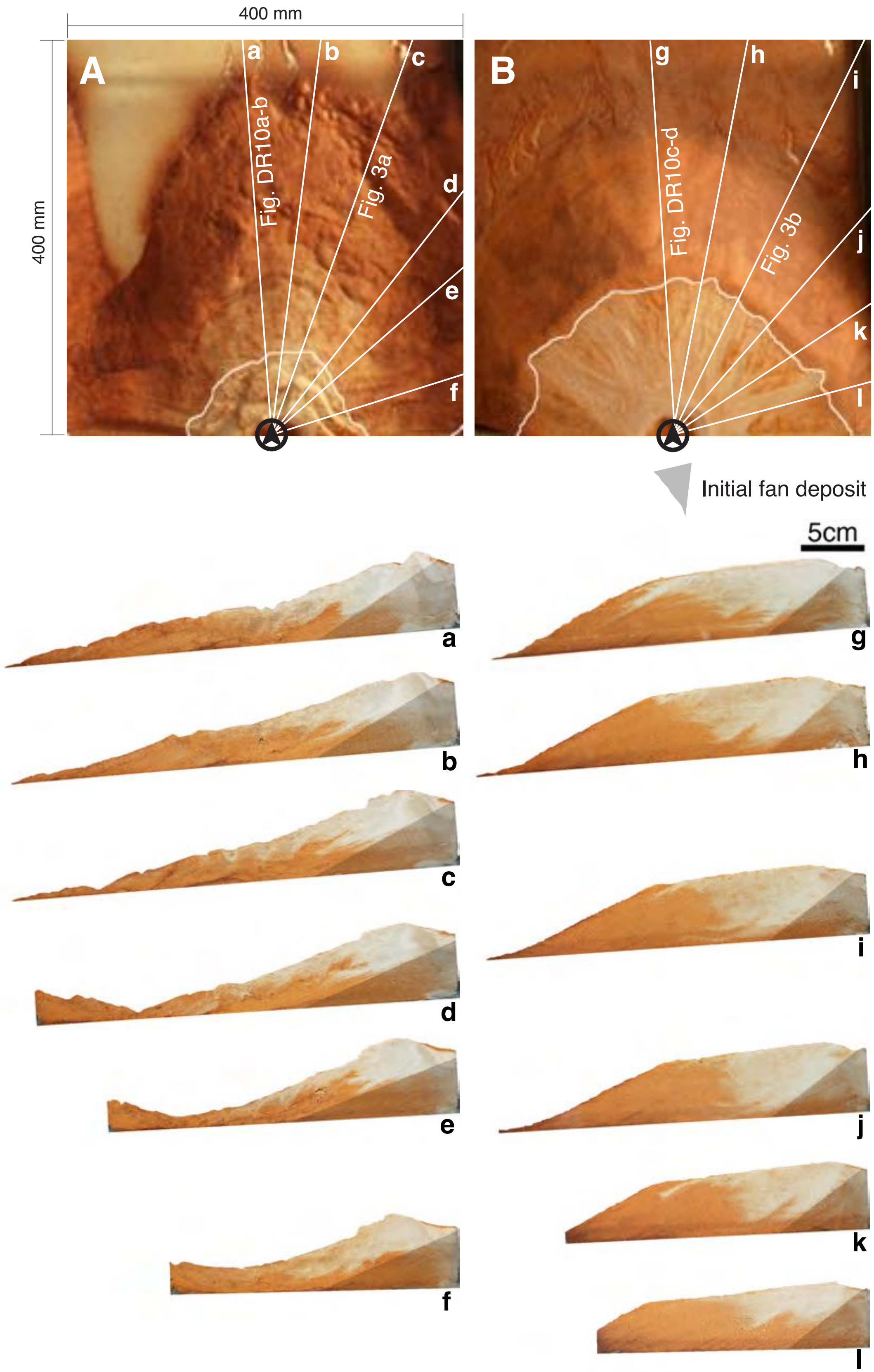

Figure Data Repository 5.

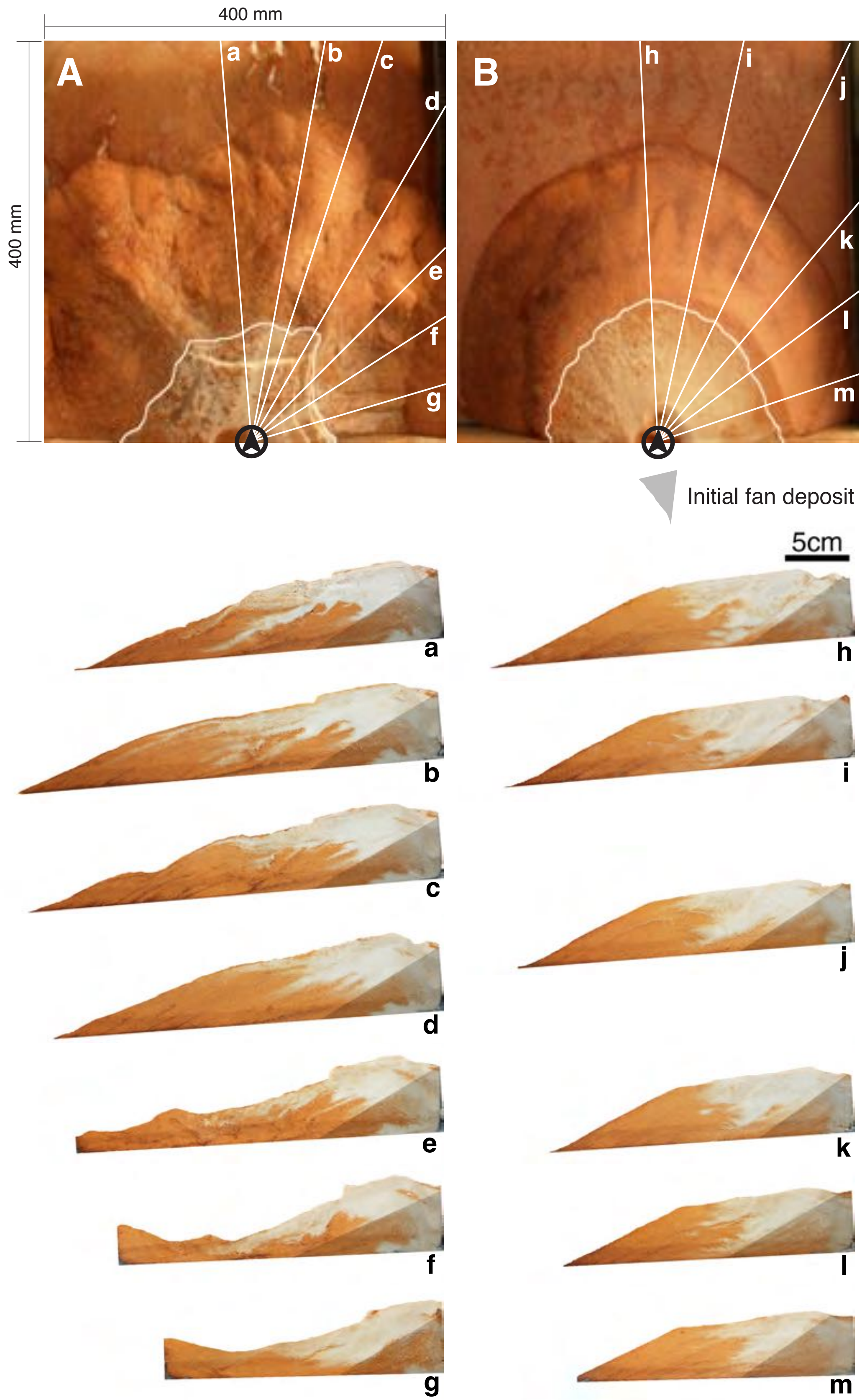

Figure Data Repository 6.

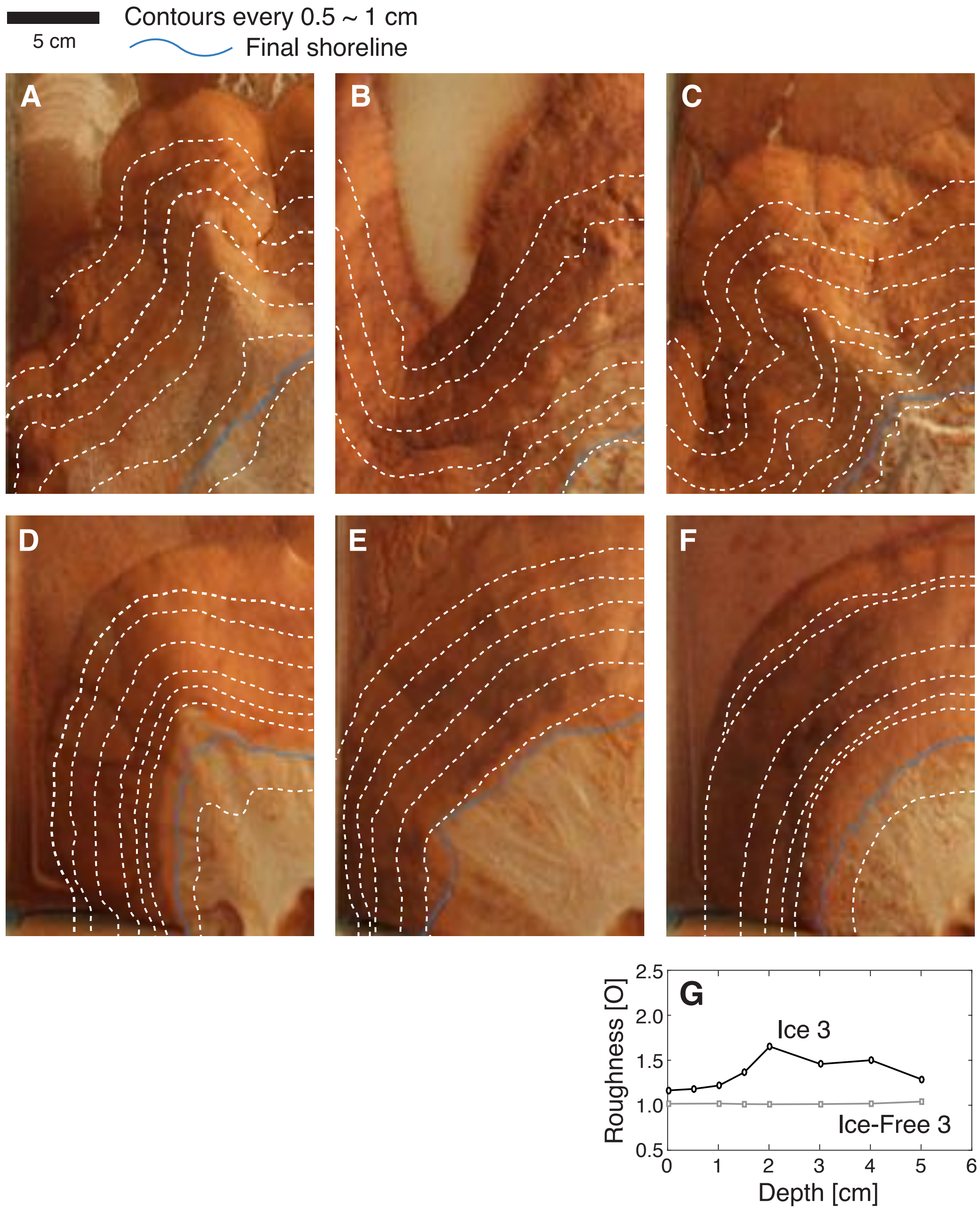

Figure Data Repository 7.

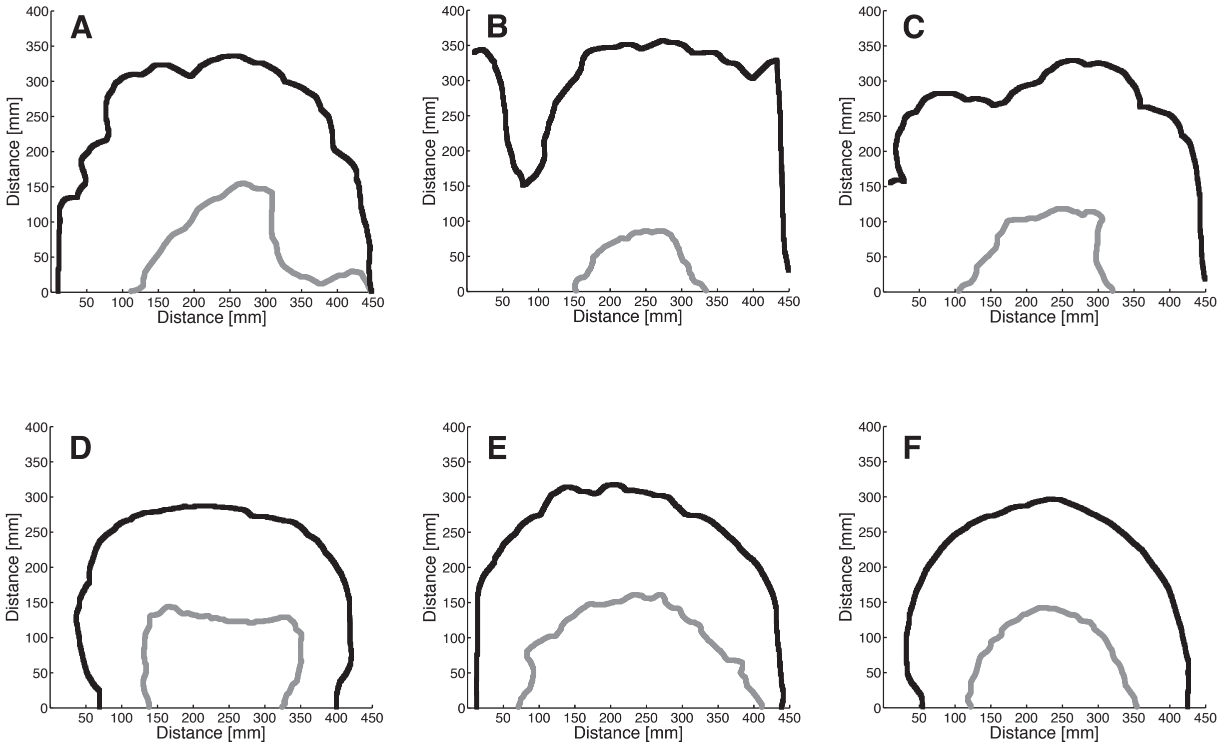

Figure Data Repository 8.

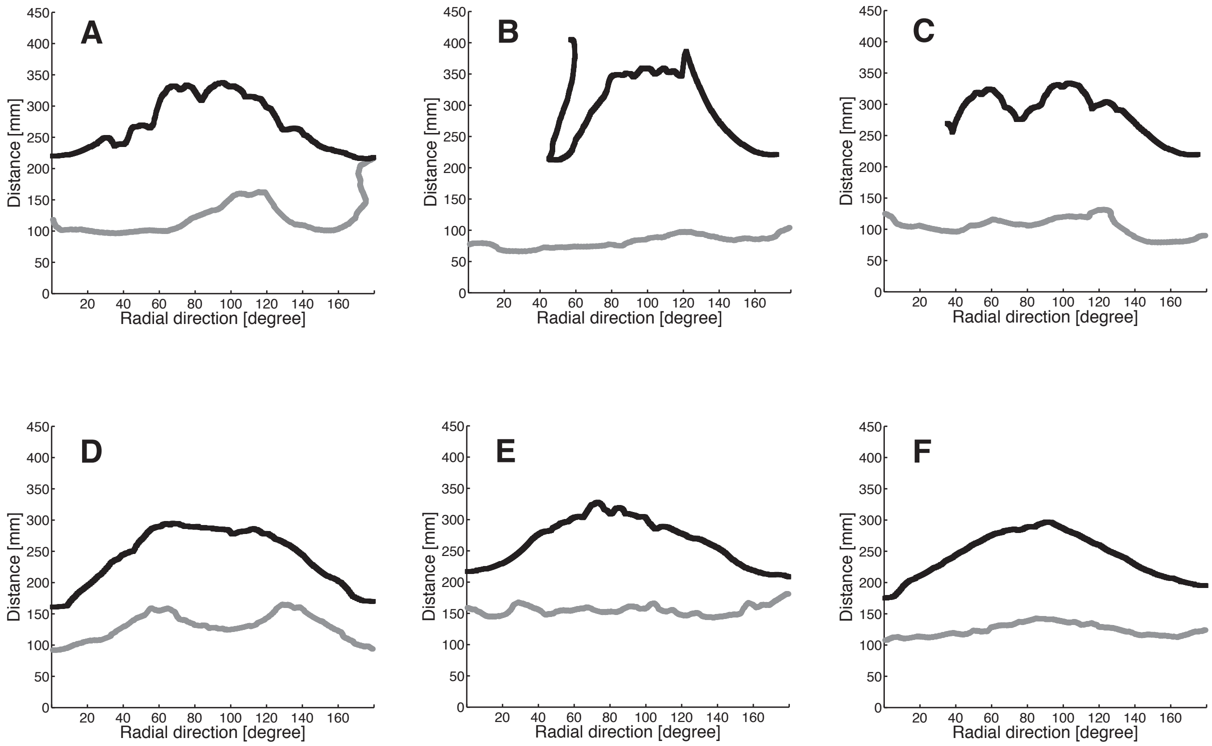

Figure Data Repository 9.

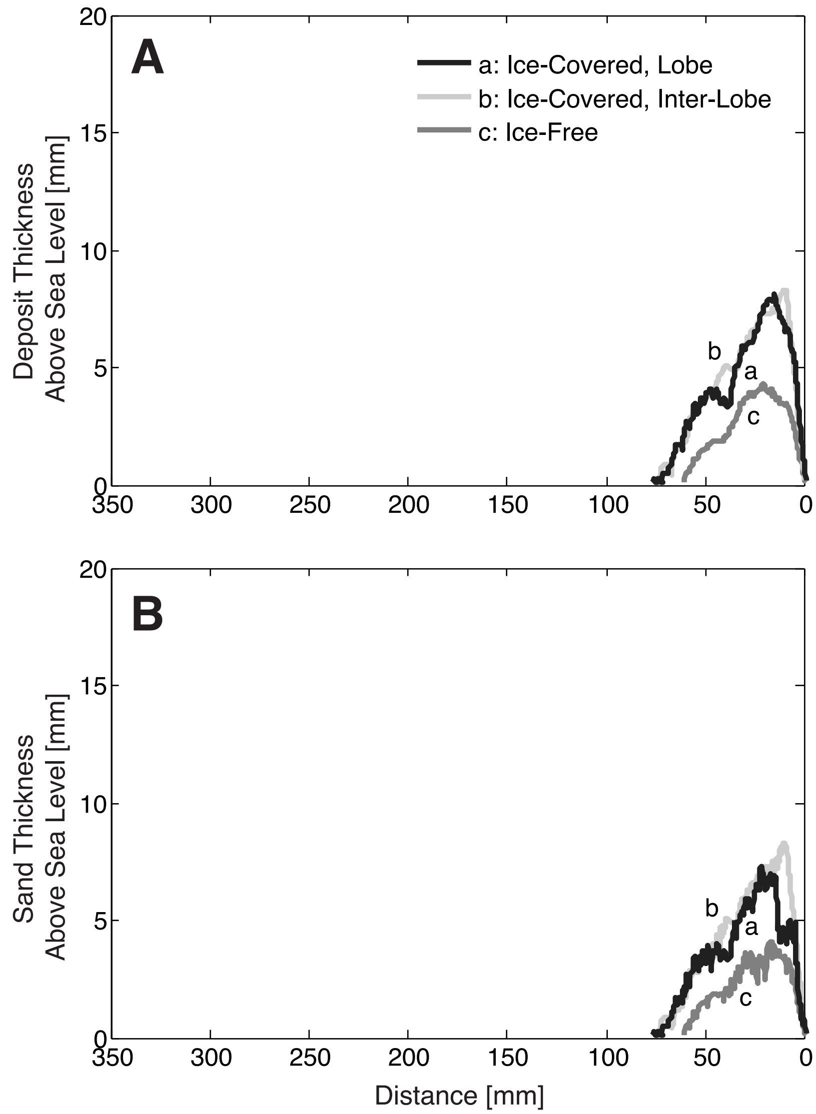

Figure Data Repository 10.

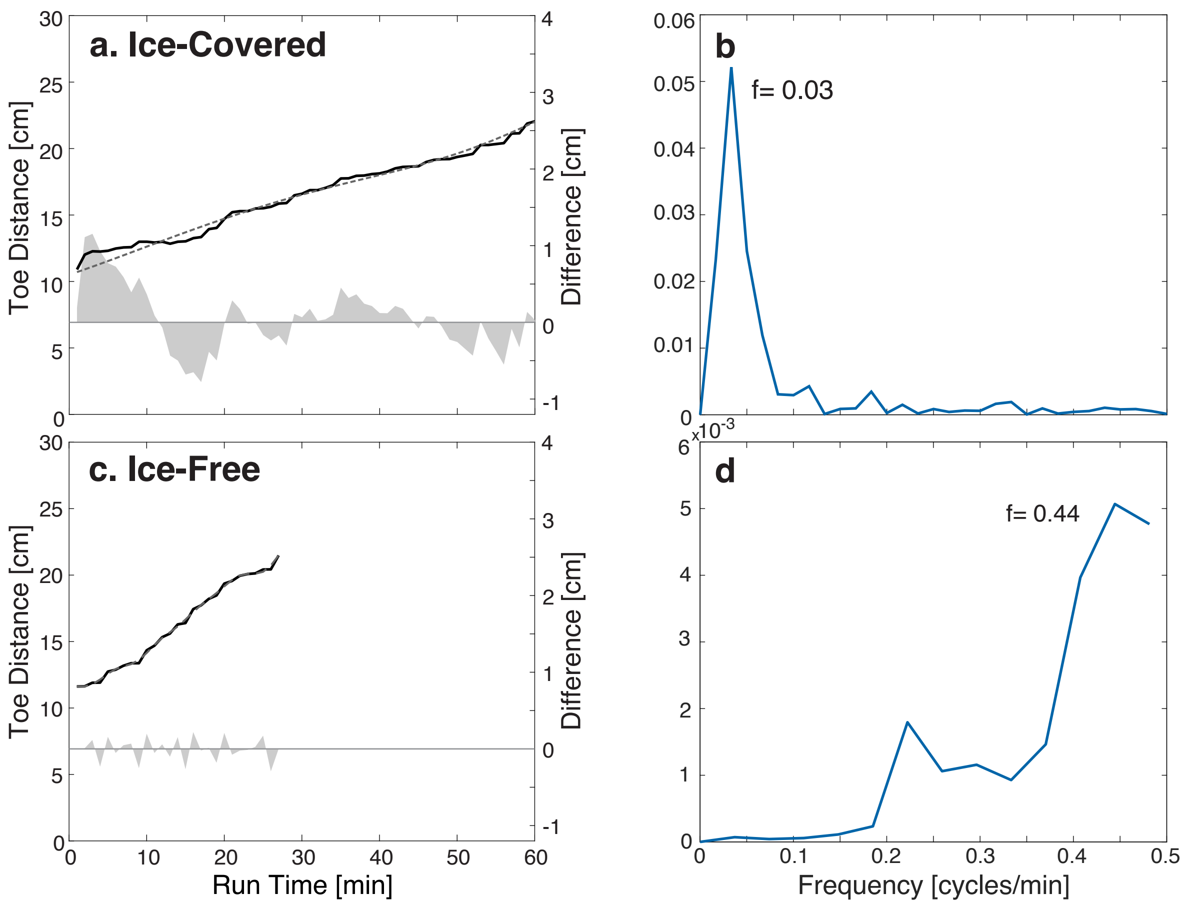

Figure Data Repository 11.

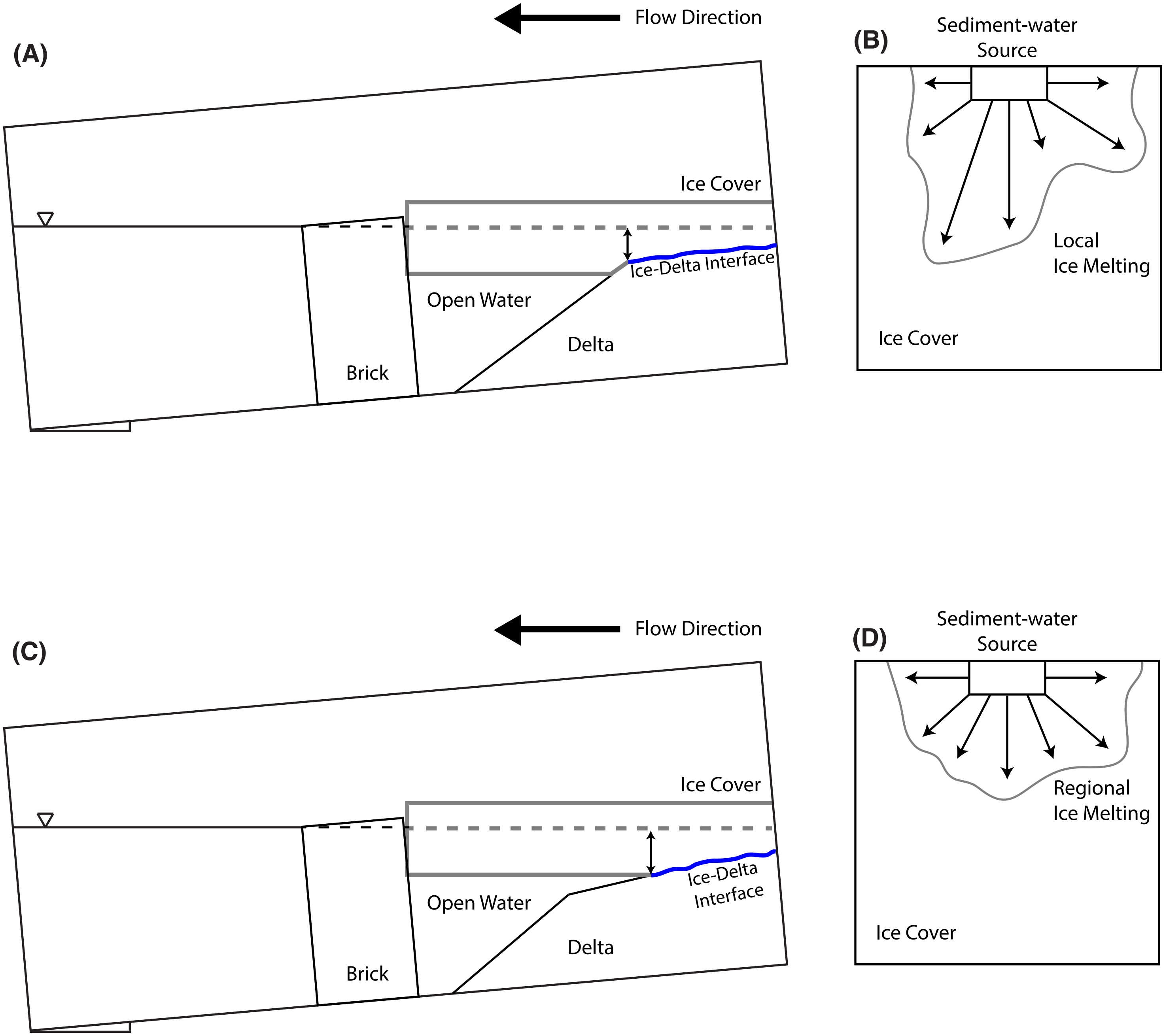

Figure Data Repository 12.

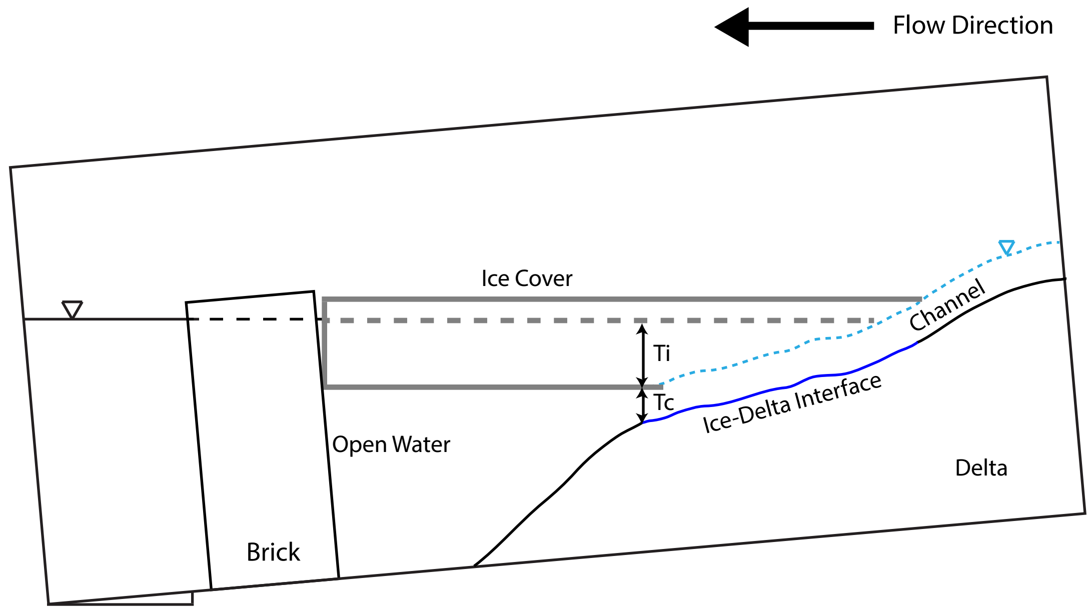

Figure Data Repository 13.

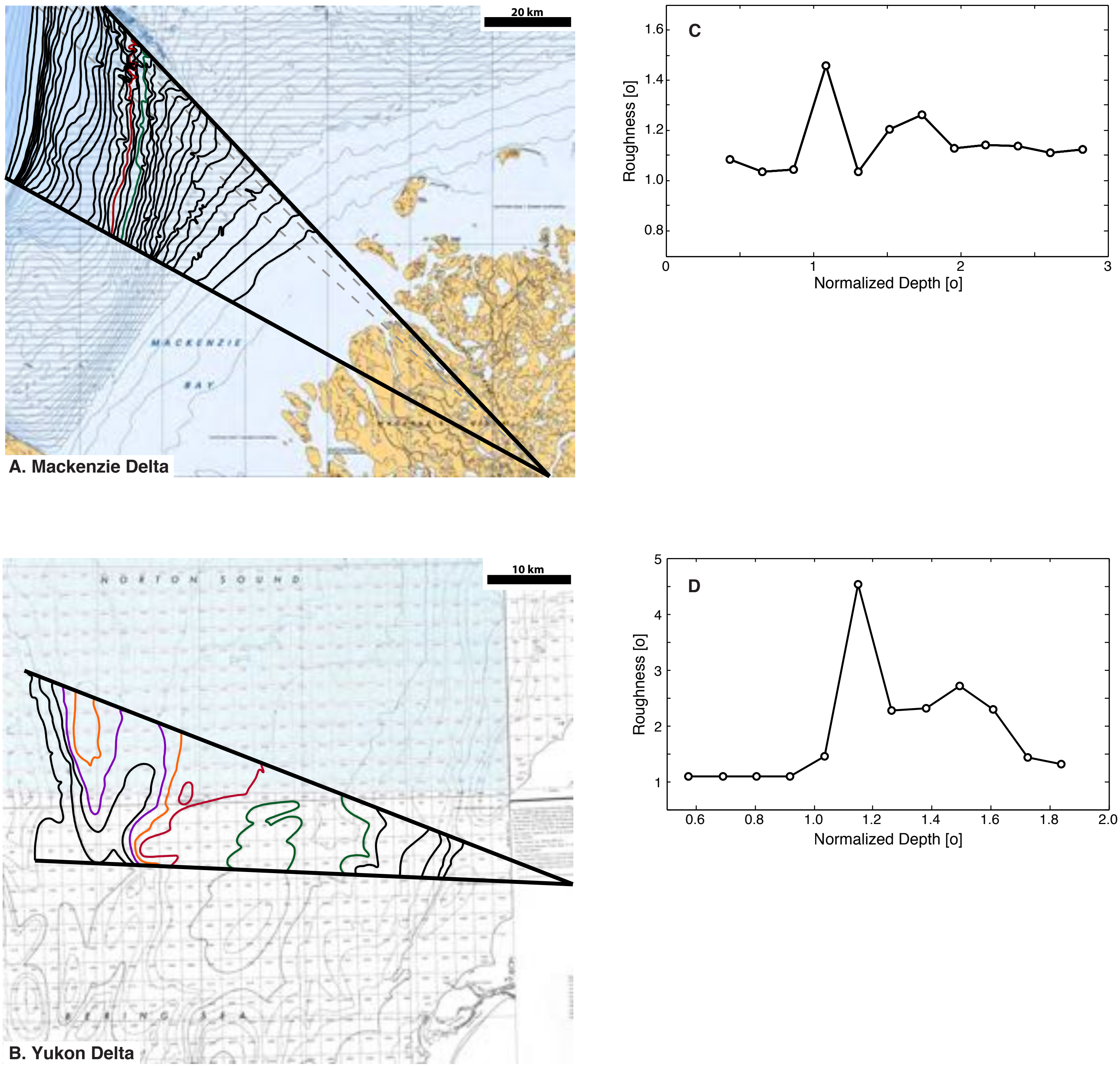

Figure Data Repository 14.

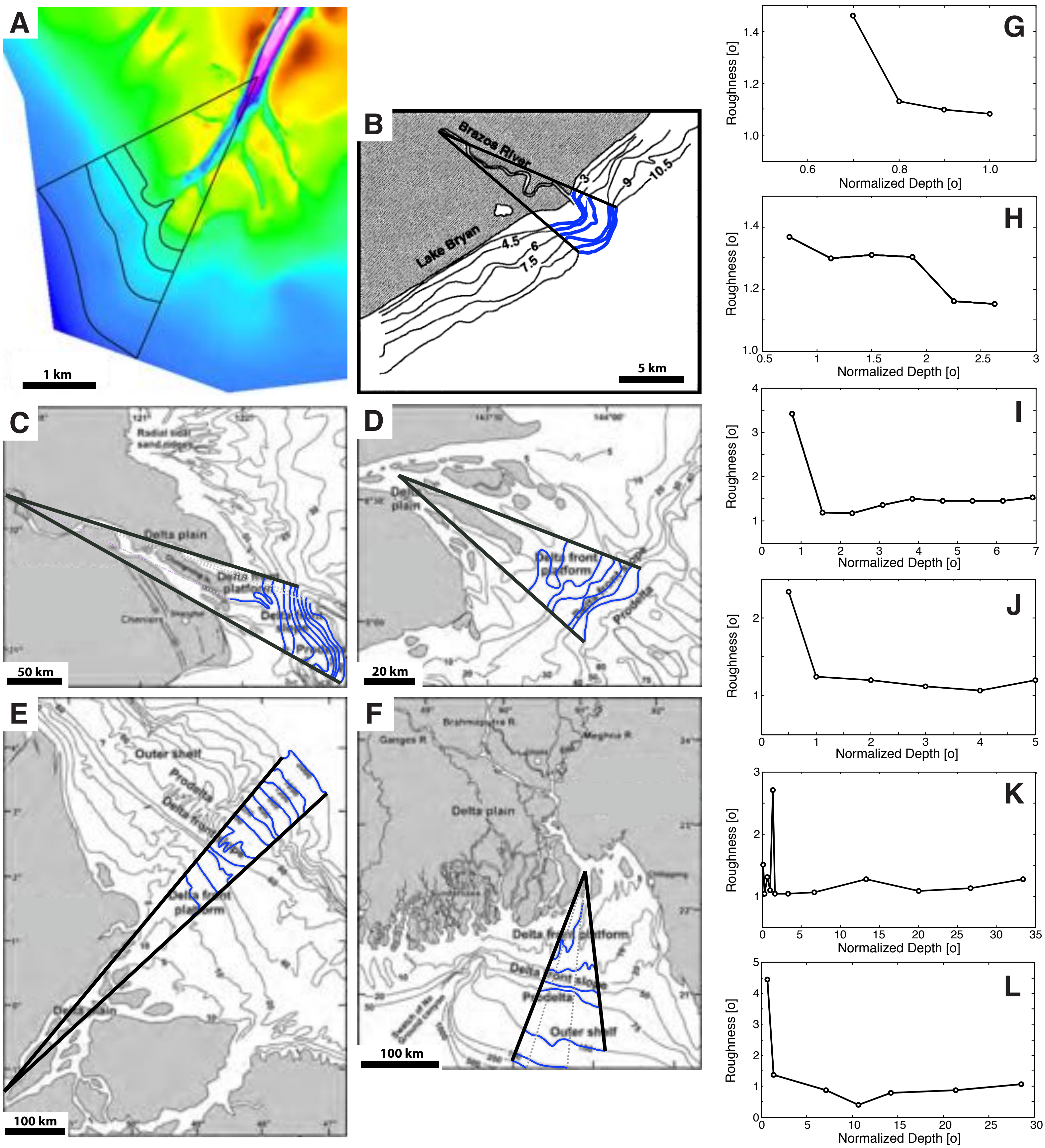

FIGURE DATA REPOSITORY CAPTIONS

Figure Data Repository 1. Schematic sketch of experimental setup with ice cover in (A) 3D and (B) cross-sectional view.

Figure Data Repository 2. Final delta deposits of each experiment. (A-C) Ice-covered deltas under (A) low (Qs = 0.228 cm^3/s), (B) high (Qs = 0.503 cm^3/s), and (C) low-to-high sediment discharge (Qs = from 0.228 cm^3/s to 0.503 cm^3/s). (D-F) Ice-free deltas under (D) low, (E) high, and (F) low-to-high sediment discharge. Solid and dashed white lines, respectively, indicate the final shorelines and delta toe positions of each deposit. (G) Distance between the shoreline (solid lines) and delta toe (dotted lines), indicating the length of subaqueous delta, and the ratio of subaqueous ice-covered delta length to subaqueous ice-free delta length (gray area) for low-to-high sediment discharge.

Figure Data Repository 3. (A-B) Final delta deposits from low sediment discharge under (A) ice-covered and (B) ice-free conditions. (a-n) Corresponding vertical stratigraphic sections of (a-h) ice-covered and (i-n) ice-free delta deposits.

Figure Data Repository 4. (A-B) Final delta deposits from high sediment discharge under (A) ice-covered and (B) ice-free conditions. (a-l) Corresponding vertical stratigraphic sections of (a-f) ice-covered and (g-l) ice-free delta deposits. Transects (a), (c), (g), and (i) show locations for Fig. DR10a-b, Fig. 3a, Fig. DR10c-d, and Fig. 3b, respectively.

Figure Data Repository 5. (A-B) Final delta deposits from low-to-high sediment discharge under (A) ice-covered and (B) ice-free conditions. (a-m) Corresponding vertical stratigraphic sections of (a-g) ice-covered and (h-m) ice-free delta deposits.

Figure Data Repository 6. Bathymetric contours overlain on half of the final delta deposits of (A-C) ice-covered deltas under (A) low, (B) high, and (C) low-to-high sediment discharge. (D-F) Ice-free deltas under (D) low, (E) high, and (F) low-to-high sediment discharge. Blue lines indicate final shorelines. (G) Surface roughness of ice-covered and ice-free deltas under low-to-high sediment discharge.

Figure Data Repository 7. Shoreline (gray lines) and delta toe (black lines) positions of (A-C) ice-covered deltas under (A) low, (B) high, and (C) low-to-high sediment discharge. (D-F) Ice-free deltas under (D) low, (E) high, and (F) low-to-high sediment discharge.

Figure Data Repository 8. Final Radial distances from the center to shorelines (gray lines) and delta toe (black lines) of (A-C) ice-covered deltas under (A) low, (B) high, and (C) low-to-high sediment discharge. (D-F) Ice-free deltas under (D) low, (E) high, and (F) low-to-high sediment discharge.

Figure Data Repository 9. (A) Subaerial deposit thickness and (B) subaerial sand thickness of stratigraphic sections through (a) a lobe and (b) inter-lobe of ice-covered delta and (c) ice-free delta from the low sediment discharge experiments. Sections are shown in Fig. 2. Letters in plots (A-B) correspond to each section in Fig. 2.

Figure Data Repository 10. Lobe-building timescales associated with sub-ice channel progradation for (a) ice-covered and (c) ice-free deltas under high sediment discharge conditions. Locations of transects, along which toe distances were measured, are shown in Fig. DR4. Solid black lines indicate measured toe distance from the apex. Dotted gray lines are the filtered data through a high-pass 5th order Butterworth filter. The differences between actual and filtered data are shown in gray area. Frequency spectra, from which timescales were computed (time=1/frequency), for (b) ice-covered and (d) ice-free deltas under high sediment discharge.

Figure Data Repository 11. Schematic sketches showing ice-sediment interaction based on (A-B) higher and (C-D) lower sediment discharges. (A) Cross-section showing the depth at which strong ice-sediment interactions occurring only at the upper part of the ice cover at shallower depths with higher discharge. (B) Plan-view showing local ice melting/erosion through sub-ice channels driving fast subaqueous progradation of the delta up against the ice cover with higher discharge. (C) Cross-section showing ice-sediment interactions over the full thickness of the ice cover with lower sediment discharge. (D) Plan-view showing slow subaqueous progradation of the delta up against the ice cover due to regional ice cover melting along the whole delta front causing continuation of the surface roughening to greater depths with lower discharge. Blue lines indicate strong ice-sediment interactions.

Figure Data Repository 12. Schematic sketch showing effective ice thickness (*Ti*) and channel depth (*Tc*) used in depth normalization. The effective ice thickness is defined as the thickness of ice cover below the sea level that is actively interacting with the delta surface.

Figure Data Repository 13. Surface roughness of Arctic deltas in natural system. (A-B) Bathymetric maps showing polygons and depth contours of (A) Mackenzie and (B) Yukon deltas, and (C-D) surface roughness of (C) Mackenzie and (D) Yukon deltas plotted against normalized depth. The area limits and opening angles were determined by associating active deltaic distributary channels and their deposit boundaries. The angle subtended by the wedge (i.e., opening angle, α), contour line length (Ls_m), and the area within each contour (Am) was measured for each polygon, and were used to compute the isometric line length (Ls_i) in order to calculate roughness. Both maps are retrieved from National Centers for Environmental Information (NCEI) of National Oceanic and Atmospheric Administration (NOAA).

Figure Data Repository 14. Surface roughness of natural deltas in temperate regions. (A-F) Bathymetric maps showing polygons and depth contours of (A) Wax Lake Delta, (B) Brazos River Delta in 1922, (C) Yangtze River Delta, (D) Fly River Delta, (E) Amazon River Delta, and (F) Ganges-Brahmaputra. (G-L) Surface roughness of (G) Wax Lake Delta, (H) Brazos River Delta in 1922, (I) Yangtze River Delta, (J) Fly River Delta, (K) Amazon River Delta, and (L) Ganges-Brahmaputra. Bathymetric maps of (A) Wax Lake Delta and (B) Brazos River delta are retrieved from Shaw et al. (2016) and Rodriguez et al. (2000), respectively. Maps of tide-dominated deltas (C-F) are retrieved from Davis and Dalrymple (2012).

TABLES DATA REPOSITORY

TABLE DATA REPOSITORY 1. EXPERIMENTAL PARAMETERS

Run name	Sediment discharge [Qs] (cm^3/s)	Water discharge [Qw] (cm^3/s)	Ice presence	Ice thickness (cm)	Basin and input water temperatures (°C)	Total run time (hours)
Main Set 1: Low sediment discharge						
Run 1	0.23	15.14	No	0	19.5	2.0
Run 2	0.23	15.14	Yes	7	3.0	2.0
Main Set 2: High sediment discharge						
Run 3	0.50	15.14	No	0	19.5	1.0
Run 4	0.50	15.14	Yes	7	3.0	1.0
Supplementary Set 3: Low – high sediment discharge						
Run 5	0.23 ~ 0.50	15.14	No	0	19.5	1.5
Run 6	0.23 ~ 0.50	15.14	Yes	7	3.0	1.5

TABLE DATA REPOSITORY 2. CHANNEL DEPTH AND ICE THICKNESS VALUES USED IN DEPTH NORMALIZATION

Name	Channel Depth (cm)	Ice Thickness (cm)
<u>Arctic deltas</u>		
Colville	350[*]	160[†]
Mackenzie	750[§]	170[†]
Yukon	1700[#]	40[**]
<u>Experimental ice-covered deltas</u>		
Ice-Covered 1	0.30	1.18
Ice-Covered 2	0.30	0.79
Ice-Covered 3	0.30	0.91
<u>River-dominated temperate deltas</u>		
Mississippi	10	N.A.
Wax Lake	2[††]	N.A.
<u>Tide-dominated temperate deltas</u>		
Yangtze	6.5[§§]	N.A.
Fly	1000[##]	N.A.
Amazon	6000[***]	N.A.
Ganges-Brahmaputra	700[†††]	N.A.
<u>Wave-dominated temperate delta</u>		
Brazos	400[§§§]	N.A.
<u>Experimental ice-free deltas</u>		
Ice-Free 1	0.30	0
Ice-Free 2	0.30	0
Ice-Free 3	0.30	0

[*]Mellor (1983)
[†]ICESat
[§]Hill et al. (2001)
[#]Chikita et al. (2002)
[**]Kovacs (1981)
[††]Shaw et al. (2016)
[§§]Saito et al. (2001)
[##]Dalrymple et al. (2003)
[***]Bouchez et al. (2011)
[†††]Coleman (1969)
[§§§]Rodriguez et al. (2000)

MOVIES DATA REPOSITORY CAPTIONS

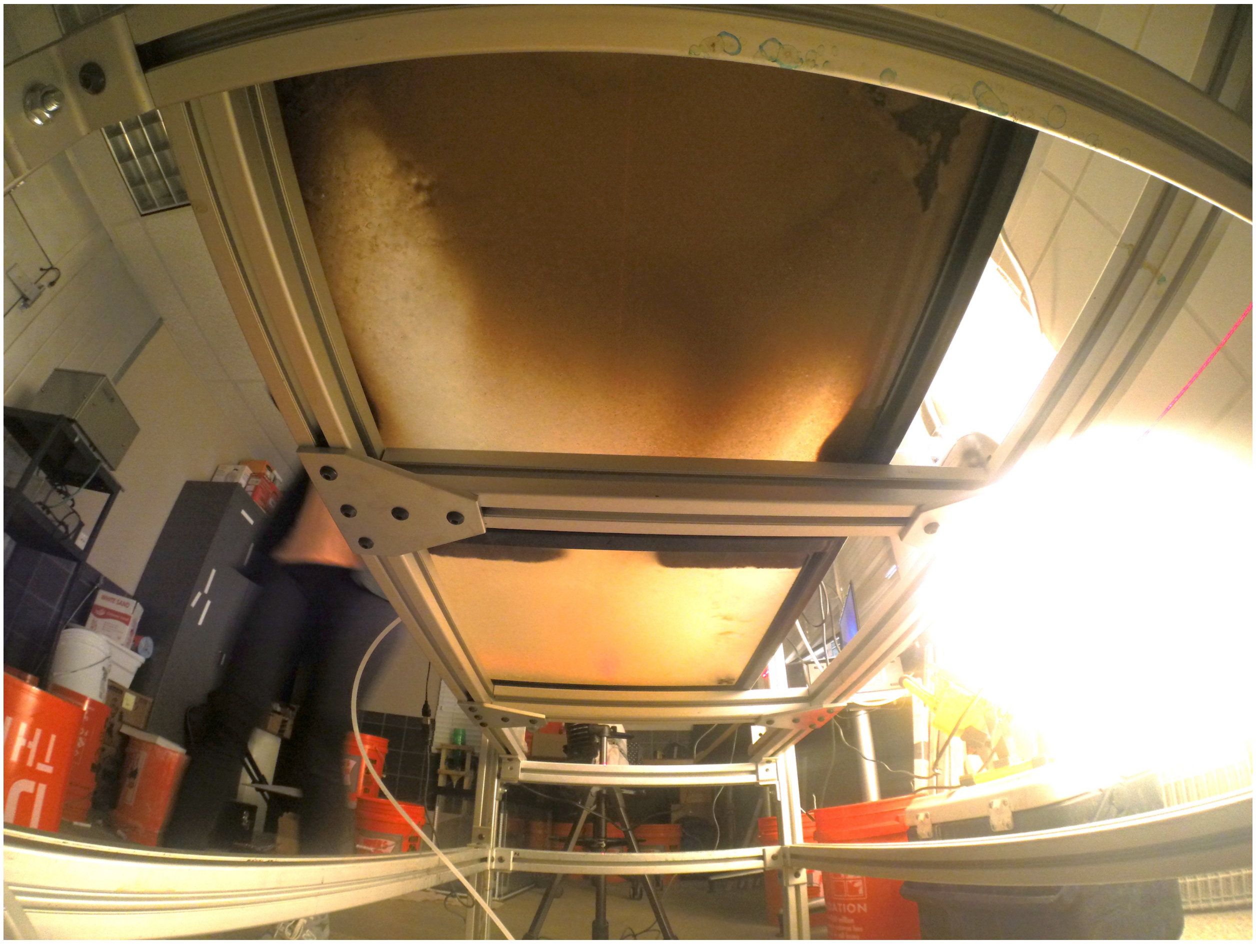

Movie Data Repository 1. Timelapse movie of experimental ice-covered delta formation from below the tank (IC_HQs). It shows ice-covered delta prograding through intermittent pulses at different locations of the delta front. 1 second in the movie is equivalent to 1 min.

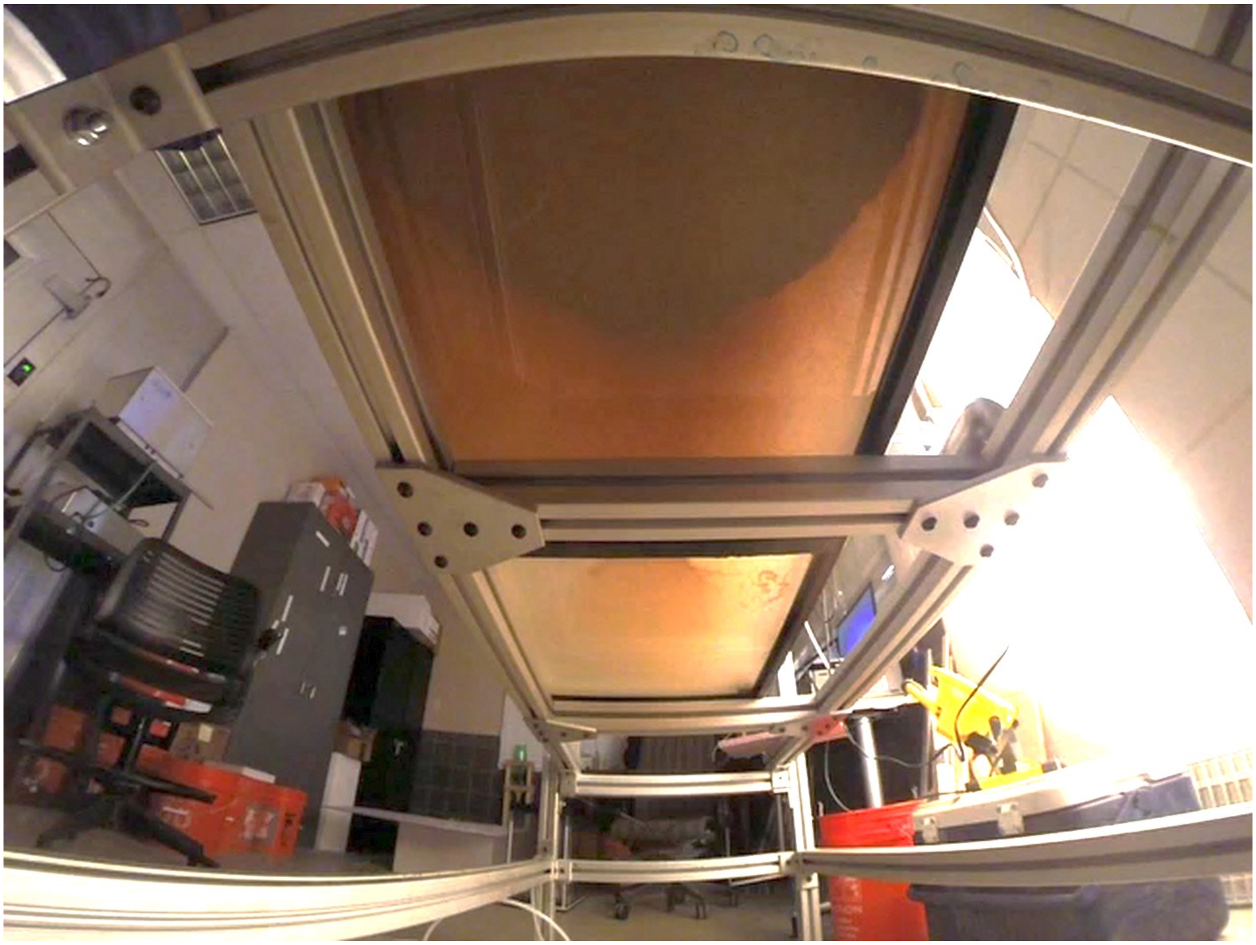

Movie Data Repository 2. Timelapse movie of experimental ice-free delta formation from below the tank (IF_HQs). It shows ice-free delta prograding uniformly in all directions through rapid lateral migration. 1 second in the movie is equivalent to 1 min.

REFERENCES CITED

Are, F., and Reimnitz, E., 2000, An Overview of the Lena River Delta Setting: Geology, Tectonics, Geomorphology, and Hydrology: Journal of Coastal Research, v. 16, no. 4, p. 1083-1093.

Bouchez, J., Gaillardet, J., France-Lanord, C., Maurice, L., and Dutra-Maia, P., 2011, Grain Size Control of River Suspended Sediment Geochemistry: Clues from Amazon River Depth Profiles: Geochemistry, Geophysics, Geosystems, v. 12, no. 3.

Chikita, K. A., Kemnitz, R., and Kumai, R., 2002, Characteristics of Sediment Discharge in the Subarctic Yukon River, Alaska: Catena, v. 48, p. 235-253.

Coleman, J. M., 1969, Brahmaputra River: Channel Processes and Sedimentation: Sedimentary Geology, v. 3, no. 2/3, p. 129-239.

Dalrymple, R. W., Baker, E. K., Harris, P. T., and Hughes, M. G., 2003, Sedimentology and Stratigraphy of a Tide-Dominaed Foreland-Basin Delta (Fly River, Papua New Guinea): SEPM, p. 147-173.

Davis, R. A., and Dalrymple, R. W., 2012, Principles of Tidal Sedimentology, Springer Science & Business Media.

Hill, P. R., Lewis, C. P., Desmarais, S., Kauppaymuthoo, V., and Rais, H., 2001, The Mackenzie Delta: Sedimentary Processes and Facies of a High-Latitude, Fine-Grained Delta: Sedimentology, v. 48, no. 5, p. 1047-1078.

Jakobsson, M., Mayer, L., Coakley, B., Dowdeswell, J. A., Forbes, S., Fridman, B., Hodnesdal, H., Noormets, R., Pedersen, R., Rebesco, M., Schenke, H. W., Zarayskaya, Y., Accettella, D., Armstrong, A., Anderson, R. M., Bienhoff, P., Camerlenghi, A., Church, I., Edwards, M., Gardner, J. V., Hall, J. K., Hell, B., Hestvik, O., Kristoffersen, Y., Marcussen, C., Mohammad, R., Mosher, D., Nghiem, S. V., Pedrosa, M. T., Travaglini, P. G., and Weatherall, P., 2012, The International Bathymetric Chart of the Arctic Ocean (IBCAO) Version 3.0: Geophysical Research Letters, v. 39, no. 12, p. L12609.

Kim, W., Paola, C., Voller, V. R., and Swenson, J. B., 2006, Experimental Measurement of the Relative Importance of Controls on Shoreline Migration: Journal of Sedimentary Research, v. 76, no. 2, p. 270-283.

Kovacs, A., 1981, Sea Ice Rubble Formations in the Bering Sea and Norton Sound, Alaska. No. CRREL-SR-81-34: United States Army Corps of Engineers Cold Regions Research and Engineering Laboratory.

Love, M. R., Caldwell, R. J., Carignan, K. S., Eakins, B. W., and Taylor, L. A., 2010, Digital Elevation Models of Southern Louisiana: Procedures, Data Sources and Analysis.

Martin, J., Paola, C., Abreu, V., Neal, J., and Sheets, B., 2009, Sequence Stratigraphy of Experimental Strata under Known Conditions of Differential Subsidence and Variable Base Level: AAPG Bulletin, v. 93, no. 4, p. 503-533.

Mellor, J. C., 1983, Upper Colville River Channel Depth Survey July 1979: Bureau of Land Management Alaska.

Rodriguez, A. B., Hamilton, M. D., and Anderson, J. B., 2000, Facies and Evolution of the Modern Brazos Delta, Texas: Wave versus Flood Influence: Journal of Sedimentary Research, v. 70, no. 2, p. 283-295.

Saito, Y., Yang, Z., and Hori, K., 2001, The Huanghe (Yellow River) and Changjiang (Yangtze River) Deltas: A Review on their Characteristics, Evolution and Sediment Discharge during the Holocene: Geomorphology, v. 41, p. 219-231.

Shaw, J. B., Ayoub, F., Jones, C. E., Lamb, M. P., Holt, B., Wagner, R. W., Coffey, T. S., Chadwick, J. A., and Mohrig, D., 2016, Airborne Radar Imaging of Subaqueous Channel Evolution in Wax Lake Delta, Louisiana, USA: Geophysical Research Letters, v. 43, p. 5035-5042.

Tal, M., Frey, P., Kim, W., Lajeunesse, E., Limare, A., and Métivier, F., 2012, The Use of Imagery in Laboratory Experiments, Fluvial Remote Sensing for Science and Management, John Wiley & Sons, Ltd, p. 299-321.

U.S. Geological Survey, 2018, National Water Information System data available on the World Wide Web (USGS Surface-Water Daily Statistics for the Nation).

Wolinsky, M. A., Edmonds, D. A., Martin, J., and Paola, C., 2010, Delta Allometry: Growth Laws for River Deltas: Geophysical Research Letters, v. 37, no. 21, p. L21403.